Electrophoretic deposition of MnCo2O4 coating on solid oxide cell interconnects manufactured through powder metallurgy

Materials & Design 227 (2023) 111768

Contents lists available at ScienceDirect

Materials & Design

journal homepage: www.elsevier.com/locate/matdes

Electrophoretic deposition of $MnCo_2O_4$ coating on solid oxide cell interconnects manufactured through powder metallurgy

Elisa Zanchi [a,*], Antonio Gianfranco Sabato [b], Mari Carmen Monterde [b,c], Lucile Bernadet [b], Marc Torrell [b], José Antonio Calero [c], Albert Tarancón [b,d], Federico Smeacetto [a]

[a] Department of Applied Science and Technology, Politecnico di Torino, Corso Duca degli Abruzzi 24, Torino 10129, Italy
[b] IREC, Catalonia Institute for Energy Research, Department of Advanced Materials for Energy Applications, Jardins de les Dones de Negre 1, Sant Adrià del Besòs, Barcelona 08930, Spain
[c] AMES PM Tech Center, Camí Can Ubach, 8., Sant Vicenç dels Horts, Barcelona 08620, Spain
[d] ICREA, Passeig Lluís Companys 23, 08010 Barcelona, Spain

HIGHLIGHTS

- Electrophoretic deposition was successfully employed to coat complex interconnects.
- Area specific resistance degradation rate of 1.2 mΩ cm^2/kh for the best coated system.
- A first comprehensive assessment of the synergy between powder metallurgy and electrophoretic deposition.

GRAPHICAL ABSTRACT

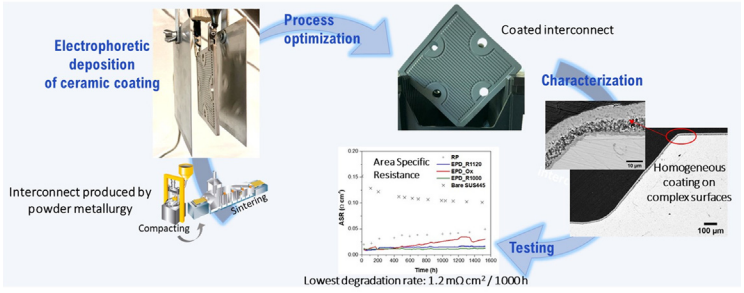

ARTICLE INFO

Article history:
Received 26 October 2022
Revised 22 December 2022
Accepted 16 February 2023
Available online 18 February 2023

Keywords:
Solid Oxide Cell
Powder metallurgy
Electrophoretic deposition
Protective coating

ABSTRACT

Developing cost-effective and durable interconnects for solid oxide cells is crucial to overcome currently existing barriers for the commercialization of this promising energy technology. A systematic microstructural and electrical characterization of $MnCo_2O_4$ spinel coatings processed by electrophoretic deposition on SUS 445 ferritic stainless steel, manufactured through powder metallurgy, is here reviewed and discussed for application in high temperature solid oxide cells stacks. The work presents a successful combination of the powder metallurgy processing of metallic interconnects with the electrophoretic deposition as a fast and versatile approach to coat complex interconnect shapes. Therefore, this study assesses the effect of the sintering route of coated steel on the final microstructure. Remarkable results in terms of electrical properties are here presented for EPD coated sample reduced at 1000 °C and re-oxidised at 800 °C in static air, obtaining an area specific resistance degradation rate of 1.2 mΩ cm^2/kh together with an effective limitation of Cr outward diffusion despite the prolonged exposure in relevant conditions. This novel approach opens the door for a new class of complex-shaped interconnects with enhanced performance and durability and excellent scalability at a low cost.

1. Introduction

The urgent need to replace conventional fossil fuels with renewable energy sources can be accomplished only through the implementation of efficient, durable and cost-competitive tech-

* Corresponding author.
E-mail address: elisa.zanchi@polito.it (E. Zanchi).

https://doi.org/10.1016/j.matdes.2023.111768
0264-1275/

nologies. Solid oxide cells (SOCs) offer a promising solution for clean energy conversion and chemical energy storage of renewable power sources. SOCs can work reversibly both in electrolysis mode (SOEC), producing hydrogen from the steam reduction with renewable electricity, and in fuel cell mode (SOFC), converting the chemical energy of hydrogen into clean electricity. Some of the SOC advantages reside in the highly efficient exploitation of electrochemical reactions, with low emissions of pollutants and fuel flexibility: indeed, not only H_2 but also CO and their mixtures (syngas) can be employed; other hydrocarbons-based fuels can broader the selection if a gas reforming system is included [1]. An important feature for SOC technology deployment is its capability to work in the reversible mode (rSOC), allowing to switch working conditions between SOEC and SOFC as needed [2]. The widespread commercialisation of SOC devices is still held back by degradation issues due to both material choice and scalability of the actual processing [3–5]. The development of more reliable and scalable processes on the different steps of SOC system fabrication will decrease the manufacturing costs helping to their rollout.

Regardless of the operation mode, SOC cells need to be connected in a stack through interconnects (ICs), which ensure gas separation and electrical connections in series or parallel. Although not directly involved in the electrochemical reactions, the interconnect is a complex component for both design and materials selection since it undergoes degradation phenomena affecting the performance of the whole stack [6]. Progress in electrolyte development and consequent reduction of the stack working temperature allowed to use ferritic stainless steel interconnects, instead of expensive, brittle and less conductive ceramic ones. Over the past two decades, a variety of expensive alloys specifically developed for IC applications have been developed: common features of these compositions involve Cr concentration >20 %, very low level of impurities such as Si and Al, the addition of alloying elements (e.g. Mn, Ti, Mo, Ni) and reactive elements (Ce, La, Y) [7,8]. Despite the complex design of the alloys, excessive oxidation or corrosion of the IC and chromium evaporation still constitute one of the major causes of stack loss of performance [9–11].

To limit degradation phenomena related to the use of stainless steel interconnects, applying a protective coating has been identified as the most practical route to ensure the requirements for their rollout as commercial industrial systems involving harsher corrosion conditions and longer working times [12]. Together with limiting the continuous chromia scale thickening and blocking Cr evaporation, the coating material must be electronically conductive at the stack working temperature, thermo-mechanically compatible with the IC and the cell, and chemically inert in selected gases. Extensive research, focused on selecting optimum materials, has identified the spinel family as the most appropriate for IC coating [13]. Among the various compositions, Mn—Co spinel (MCO) has received special attention thanks to improved functional properties, adequate coefficient of thermal expansion, and sufficient electrical conductivity [14,15].

Research conducted so far on developing spinel coating materials allows to include cheaper commercial alloys - i.e. with lower Cr addition and higher impurities content - among promising IC materials; some examples are AISI 441 (~18 % Cr) [16–18], but also AISI 430 (~16 % Cr) [19,20]. However, the total cost of the interconnect is affected not only by the steel composition, but largely by manufacturing and coating processing routes; therefore, the implementation of affordable and scalable production methods is still strictly required.

Metallic interconnects are typically produced by conventional lamination, forming and machining manufacturing techniques, however, powder metallurgy (PM) may represent an attractive alternative. Powder Metallurgy (PM) presents near-*net*-shape capabilities and a good surface finishing, even with complex geometries. In addition, it is cheaper than conventional manufacturing techniques since reduces the post-sintering processes while decreasing the wasted material compared with machining. Indeed, the energy costs of processing using PM can be estimated to be 7 kWh/Kg compared to >10 kWh/Kg for processing by stamping metal sheet with lamination and subsequent machining (15 kWh/Kg) [21], leading to a lower carbon footprint of the product in manufacturing using conventional PM. The typical designs of IC are exceptionally suitable to be processed via PM with almost no need for additional manufacturing steps. Up to now, only a few studies focused on PM for metallic IC [22–24] mainly focused on the PM of Crofer22APU ferritic stainless steel and still leaving room for improvement in terms of densification of the achieved interconnects.

Due to the complex geometry of the type of interconnects required for ensuring an optimal gas distribution through the channels, the coating deposition technique should be properly selected to ensure the protection of the different surfaces. To this purpose, electrophoretic deposition (EPD) is considered a promising route, also when compared with other deposition methods such as sputtering, dip coating or thermal evaporation [13,25,26]. Electrophoretically deposited coatings have been produced in a series of different Mn—Co and Mn—Cu spinel compositions and tested under various working conditions in the recent years [14,27–31]. The great advantage of the EPD technique resides in the possibility to deposit homogenous conformal coatings in a few seconds and at room temperature (RT). Moreover, EPD offers wide versatility for material to be deposited: for example, Cu-doped MCO [32], Fe-doped MCO [33,34], as well as Cu—Fe-doped MCO [31] obtained by single step co-deposition of $Mn_{1.5}Co_{1.5}O_4$, CuO and Fe_2O_3 mixed in desired ratios. Thanks to the versatility of materials employed and coatings morphology, as well as the low-energy demand, EPD is considered a suitable technique for industrial applications in SOC technology. The simple and adaptable EPD set-up enables the scaling-up from laboratory samples to real-size interconnect: indeed Crofer22APU interconnects coated with MCO coating deposited by EPD and tested in a stack at 850 °C have already demonstrated excellent behaviour in terms of both oxidation resistance, Cr-poisoning and stability over time [35].

After the deposition, the optimisation of the coating sintering step appears also as one of the key factors to take into consideration [27]. High densification is ensured by a two-step reactive sintering. On the other hand, single oxidation in air can be performed during the stack consolidation treatment, lowering the achieved densification but still ensuring the protective behaviour and Cr retention capability of the coating [36,37].

The present study represents the first attempt to integrate the powder metallurgy approach - a near-*net*-shape interconnect production perspective - with electrophoretic deposition - a fast and versatile coating deposition method – in the processing of SOC metallic interconnects. SOC interconnects have been produced by powder metallurgy with SUS 445 ferritic stainless steel with a Cr content of ~20 %. The alloy SUS 445 was selected as the result of a first preliminary study (not reported here) between different alloys, taking into consideration the Cr content (>20 %) necessary to ensure high corrosion resistance, as well as the processability of the alloy in form of powder first and then as sintered components. Indeed, the density of the final component is a key factor in powder metallurgy, especially when the final application as SOC interconnect is considered: in this case the powders of the selected alloy allowed to reach a density >96 % with the optimized sintering treatment. In the present study, the interconnects produced by PM have a final thickness of 1.9 mm. Manganese-cobalt spinel coating has been processed by EPD and subjected to different post-deposition treatments to recreate conditions of possible

industrial applications scenarios. The performance of the IC-coating systems has been evaluated in terms of area specific resistance for a total time of 1500 h.

2. Experimental

2.1. Samples preparation

Stainless steel interconnects with a dimension of 80 × 80 × 2. 5 mm were produced by AMES PM (Barcelona, Spain) using SUS 445 (Cr = 20.00–22.00 wt%, Mn = 0.61–0.69 wt%, Mo = 1.1–1.13 w t%, Si = 0.01–0.33 wt%, trace of C, P and S; Fe = Bal.) powder as a feedstock material. Selected powders were pressed in a cermet die with uniaxial pressure of 300 MPa at room temperature and afterwards sintered on cordierite-mullite ceramic plates at 1285 °C for 90 min under 100 % hydrogen atmosphere.

Commercial $MnCo_2O4$ spinel powder (MC12) from KCeracell (South Korea) was used as feedstock material for the deposition of the protective coating. For the electrophoretic deposition, 0.5 g/l of I_2 was dispersed in a solution of 50 vol% ethanol/50 vol % acetone; afterwards, 15 g/L of MC12 was added and dispersed by sonication and magnetic stirring for around 20 min to obtain a stable suspension. Before EPD, SUS 445 IC were cleaned in ethanol/acetone for 10 min in an ultrasonic bath. Deposition parameters were optimized at 50 V for the 30 s maintaining the sample-electrode distance fixed at 15 mm. Three-electrode setup was used to coat both sides of the IC in a single step process displayed in Fig. 1a. After drying, samples were sintered under three different procedures to be compared. A batch of IC, labelled as EPD_Ox, was subjected to an oxidative sintering process for 5 h at 800 °C in static air (2 °C/min). The second batch underwent a two-step sintering, with a first reduction treatment at 1000 °C for 2 h in a tubular furnace in flowing H_2 2 vol%, heating/cooling ramps of 10 °C/min followed by a re-oxidation step at 800 °C for 5 h under static air; these samples are in the following labelled as EPD_R1000. The third group of samples was reduced at 1120 °C for 15 min only, in flowing H_2 5 vol%, heating/cooling ramps at 26 °C/min and therefore labelled as EPD_R1120. The three selected sintering procedures were chosen to simulate typical sintering conditions applied in continuous furnaces at the industrial level. EPD was demonstrated to be effective also for coating real dimension ICs (see Fig. 1b).

To better evaluate EPD performance as a valuable deposition method, additional steel coupons were coated by the roll painting (RP) technique at AMES PM. A terpineol-based ink was prepared with MC12 and 4 subsequent depositions were performed on the steel samples. After drying, sintering was carried out in an industrial continuous furnace (CREMER) in H_2 5 vol% at 1120 °C for 15 min.

Table 1 provides an overview of the fabrication conditions of the different types of coated samples.

2.2. Characterization techniques

As prepared EPD-coated samples were subjected to preliminary characterization after each sintering step (reduction, re-oxidation or simple oxidation). X-ray diffraction (XRD) patterns were obtained using a Bruker D8 diffractometer with Cu-Kα radiation, recorded at room temperature in a 2Theta range of 10°–70°, with a step size of 0.02626° and time per step of 10.20 s; recorded patterns were analysed using HighScore Plus PANalytical software and JCPDS PDF-2 database [38]. Morphological and compositional characterizations were carried out by a field-emission scanning electron microscope (FE-SEM; SupraTM 40, Zeiss, Oberkochen, Germany) equipped with an energy dispersive X-ray analyser (EDX, Bruker, Germany). Samples were embedded in epoxy resin and polished up to 4000 SiC paper to reveal the cross-sections.

Area specific resistance (ASR) was measured on 10 × 20 mm^2 samples obtained from coated IC using a 4-probe method on each couple of coupons. The electrical connection was realized by welding Pt-wires. Every sample was made up of the two coupons placed one over the other ensuring the contact within the crests of the channelled surface (Fig. 1c). The electrical connection between the two coupons was obtained by manually deposition of Pt-paste. Therefore, the contact area considered in the calculation of the ASR corresponded to the sum of the crests of each interconnect coupon (i.e., 1 cm^2). The resistance was measured by applying a constant current density of 400 mA cm^{-2} and measuring the voltage drop over each couple of coupons. The measurement was carried out at 800 °C in static air during 1500 h. To calculate the ASR, the considered area was the one strictly corresponding to the contact, therefore the area corresponding to the crests. Post-mortem morphological, microstructural and compositional characterization was carried out on cross-sections using FE-SEM and EDX.

3. Results and discussion

3.1. Characterization of as-prepared coatings

Overall, the whole set of samples presented homogeneous and complete coatings (Fig. 1b). In order to study the crystalline phases after the different sintering processes, XRD was performed on the thermally treated samples. Fig. 2 shows the comparison of X-ray diffraction patterns obtained for the EPD deposited samples after the reducing step, performed at different parameters: EPD_R1000 and EPD_R1120 samples. Interestingly, XRD reveals that despite the different temperatures, time and atmospheres, both samples present identical phases, consisting of MnO (PDF #07-0230, cubic)

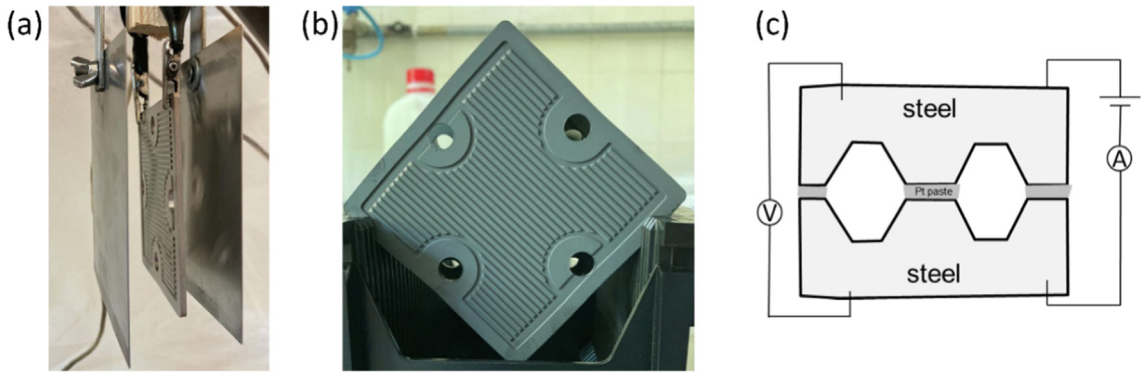

Fig. 1. Images of the EPD set-up with IC before (a) and after (b) coating deposition; (c) sketch of electrical connections for characterization of the Area Specific Resistance.

Table 1
Samples overview.

Coating deposition	Sample label	Reduction treatment	Oxidation treatment
EPD 50 V, 30 s	EPD_R1000	1000 °C, 2 h, H_2 2 %	800 °C, 5 h, static air
	EPD_R1120	1120 °C, 15 min, H_2 5 %	(In situ for ASR test)
	EPD_Ox	–	800 °C, 5 h, static air
Roll painting 4 depositions	RP	1120 °C, 15 min, H_2 5 %	800 °C, 5 h, static air (In situ for ASR test)

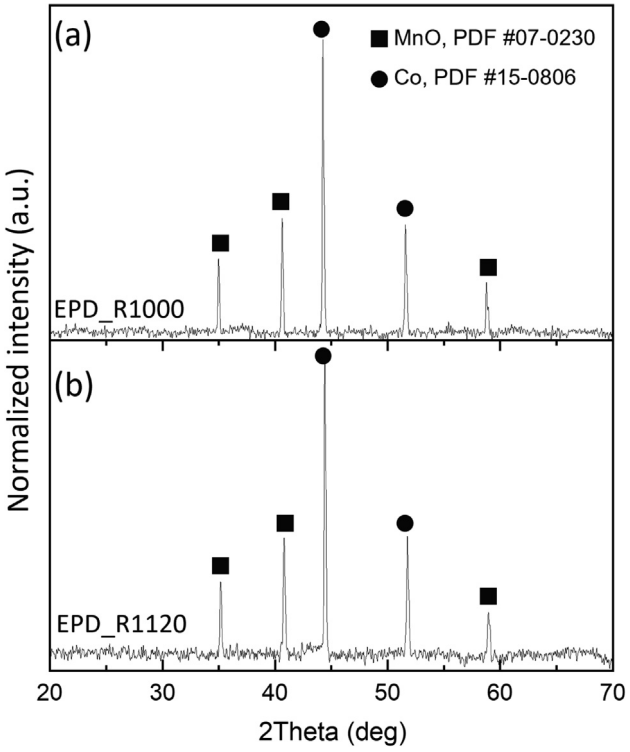

Fig. 2. XRD patterns of EPD_R1000 coating (a) and EPD_R1120 coating (b); phase identification of MnO (squares) and Co (circles) as included in the PDF Database.

and metallic Co (PDF #15-0806, cubic), which indicates that the MC12 powder was completely reduced in both cases. Similar XRD patterns were obtained in previous studies on the EPD deposition of $Mn_{1.5}Co_{1.5}O_4$ powder [31,33]. Therefore, treating deposited MC12 powder at 1000 °C with 2 vol% H_2 (not flammable mixture) is sufficient to completely reduce the original spinel phase.

Despite showing similar XRD patterns, EPD_R1000 and EPD_R1120 exhibit clear differences at the morphological level after the reducing treatment, displayed by FE-SEM cross-sections in Fig. 3. Backscattered electrons imaging allows distinguishing Co and MnO since brighter spots correspond to metallic Co particles while grey zones are related to the MnO phase. As noted in Fig. 3a and c, both coatings are homogeneously deposited and attached presenting a thickness of around 15 μm. One can conclude that EPD deposited coatings resulted to be very effective in covering the complex shapes of the interconnect surface (including both convex and concave features). EPD_R1120 coating is remarkably denser presenting better attachment to the steel substrate than EPD_R1000 layers (comparison between Fig. 3d and b, respectively). Indeed, reducing treatments at higher temperatures led to enhanced coarsening of metallic cobalt particles, despite the rapid treatment profile. In addition, EPD_R1120 samples also show more pronounced oxidation as suggested by the darker contrast layer at the steel/coating interface (Fig. 3d). Regarding chromium diffusion into the EPD barriers, dark grey regions in EPD_R1120 (as the one labelled as d3 in Fig. 3d) were evaluated by EDX containing high values of Cr (around 17 at.%), together with the relevant concentration of Mn and Co, which proves substantial diffusion and reaction of chromium with the coating element. The Mn/Co ratio in areas labelled as d1 and d2 also in Fig. 3d show a slightly higher Co content in the outer part of the coating, where the chromium concentration (>1 at.%) suggests that small Cr evaporation phenomena possibly occurred during the treatment at 1120 °C. On the contrary, EDX analysis on the EPD_R1000 sample marked in Fig. 3b, indicates that the Mn/Co ratio is higher than expected in the inner region of the coating. The composition of point labelled as b3 in the Fig. 3b, collected on the middle of the oxide scale, points out a more intense presence of Mn than Co. Moreover, the significant Fe content coming from the interaction of the steel substrate further proves that the oxide scale is thinner than for the EPD_R1120 sample. Although EDX quantification at the interface is not fully consistent on the identification of oxide scale thickness, the comparison between EDX at the oxide scale of point b3 and d3, together with morphological evidence discussed above, proves that performing the reducing treatment at 1120 °C for only 15 min strongly affects the reactions at the interfaces compared to a 2 h-treatment at 1000 °C.

Few studies have investigated the microstructure evolution of Mn—Co spinel coatings after the reducing sintering step. For example, the present authors in a previous paper [33] showed that increasing the reduction temperature from 900 °C to 1000 °C of Fe-doped $Mn_{1.5}Co_{1.5}O_4$ spinel improves the coating densification. Lower Co relative content in the $Mn_{1.5}Co_{1.5}O_4$ spinel led to less intense Co coarsening phenomena at 1000 °C compared to the case of the present study (EPD_R1000 sample). In the study of Bobruk et al. [37], sintering parameters of $MnCo_2O_4$ spinel were more deeply discussed from 900 °C to 1100 °C (thermal treatments were performed for 2 h at different steam content) showing a clear temperature dependence on the cobalt coarsening. Indeed, in the present study, Co particles agglomeration is already detected after 15 min at 1120 °C.

Fig. 4 reports X-ray diffraction patterns of EPD coatings recorded after oxidation treatment (EPD_Ox) or re-oxidation step (EPD_R1000 and EPD_R1120 samples), in all cases performed at 800 °C for 5 h in static air. As a benchmark, the diffraction pattern of MC12 as-received powder is also reported (Fig. 4d). A single-phase cubic spinel is identified (PDF #23–1237). The diffraction pattern obtained for the EPD_Ox coating (Fig. 4a) corresponds with the $MnCo_2O_4$ phase in agreement with the as-received MC12 powder; narrower diffraction peaks indicate the presumable grain growth promoted by oxidation. Cubic spinel is also the only crystalline phase detected in EPD coatings subjected to two-step sintering but different relative intensity of diffraction peaks is observed. In this regard, EPD_R1000 (Fig. 4b) shows stronger intensity of peak at 30.5°, corresponding to the (220) plane. This effect is further enhanced for the EPD_R1120 sample (Fig. 4c) where both (220) and (440) planes become the first and second most intense, respectively. This suggests that MC12 powder subjected to two-step sintering forms a cubic spinel structure with preferred (110) crystal orientation and that the degree of orientation is influenced by the parameters of the reducing heat treatment. Coating reduced at higher temperatures with faster heating/cooling ramps presents the most significant preferential orientation. In this same direction, Talic et al. [39] previously reported a certain preferential

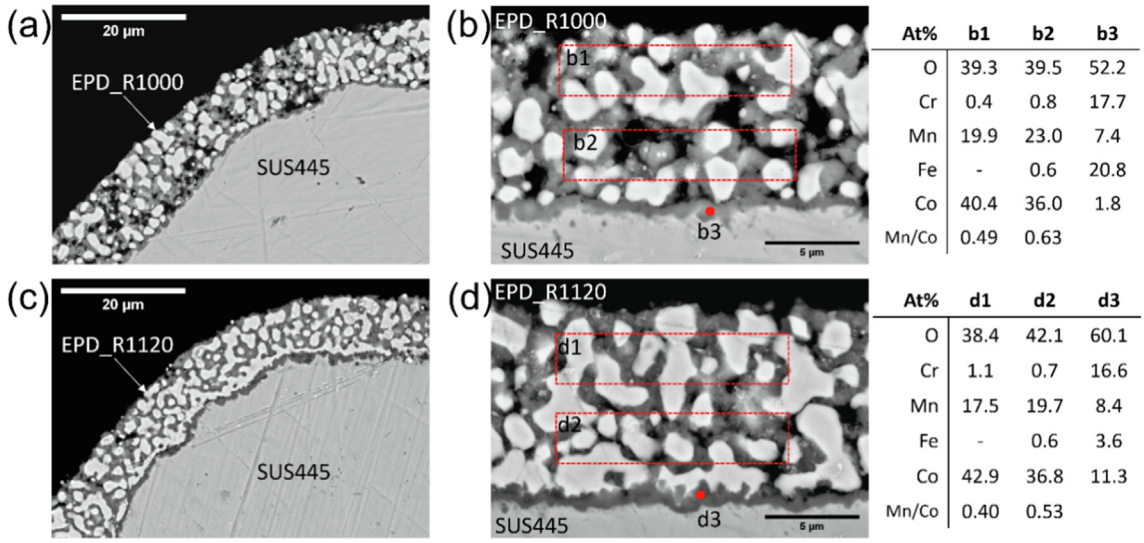

At%	b1	b2	b3
O	39.3	39.5	52.2
Cr	0.4	0.8	17.7
Mn	19.9	23.0	7.4
Fe	-	0.6	20.8
Co	40.4	36.0	1.8
Mn/Co	0.49	0.63	

At%	d1	d2	d3
O	38.4	42.1	60.1
Cr	1.1	0.7	16.6
Mn	17.5	19.7	8.4
Fe	-	0.6	3.6
Co	42.9	36.8	11.3
Mn/Co	0.40	0.53	

Fig. 3. FE-SEM cross-section images (backscattered electrons) at different magnifications of coatings after reduction treatment, with EDX elemental analysis of regions and points marked in the red colour of EPD_R1000 (a,b) and EPD_R1120 (c,d) samples.

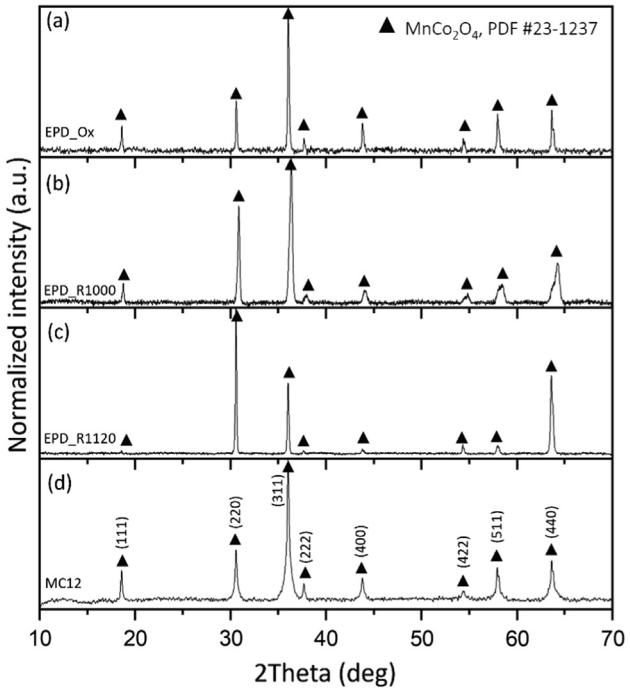

Fig. 4. XRD patters of EPD_Ox coating (a), EPD_R1000 coating after reoxidation (b), EPD_R1120 coating after reoxidation (c) and MC12 powders (d) indexed in cubic unit cells according to $MnCo_2O_4$ phase as included in the PDF Database.

orientation of EPD deposited Mn—Co spinel reduced at 1100 °C and re-oxidised at 800 °C.

The morphology of all EPD coatings after the sintering process is reported in Fig. 5, where overviews at low magnification (a, d, g) are presented to appreciate the uniformity of the coatings in different parts of the interconnect, especially in the most critical areas with concave (b, e, h) or convex (c, f, i) features. After the re-oxidation treatment, the EPD_R1000 coating is 15–20 µm-thick, it is well densified and remains perfectly attached to the steel substrate. As clearly observed in Fig. 5c, outer areas of the coating appear especially densified, as well as the inner 2 µm-thick regions of the coating close to the interface with the steel. EDX elemental analysis revealed negligible Cr content and a close to nominal Mn/Co ratio throughout the whole coating.

On the other hand, the EPD_R1120 sample (Fig. 5d–f) exhibits clear uneven coating densification, despite being continuous and presenting good adhesion to the steel substrate. As observed in Fig. 5f, the EPD_R1120 coating after re-oxidation presents two different morphologies: the outer area, which is fully dense, and the inner layer with lower density. This morphology has not been identified in previous works on coatings deposited by electrophoretic deposition. More often, the EPD coatings present a thin (few microns) densified layer at the interface with the steel while, when the maximum temperature of the reducing treatment is 1000 °C, some coatings keep a residual porosity distributed on the outer part [27,30]. On the other hand, for higher temperature of the reducing sintering step, Bobruk et al. [37] showed similar characteristics of $MnCo_2O_4$ reduced at 1100 °C for 2 h and subsequently re-oxidised at 900 °C for 2 h. Interestingly, similar results were obtained in the case of the EPD_R1120 sample despite the much shorter time of the reduction treatment (15 min). EDX elemental analysis of areas marked in Fig. 5f shows that the Mn/Co ratio of EPD_R1120 remarkably differs from the nominal value, pointing out that porous inner layers are rich in Co while dense outer regions are rich in Mn. Overall, the reducing treatment carried out at 1120 °C resulted in the formation of bigger Co particles; during the re-oxidation treatment, the formation of the spinel and its consequent densification ended up with a different distribution of porosity between the outer and the inner part of the coating. It can thus be suggested that an uneven Co particles dimension and relative distribution determined a different kinetic of the reaction mechanism with the MnO and the oxygen during the re-oxidation treatment, thus triggering the reaction from the outer layer and the consequent different densification of the spinel phase.

Finally, images of EPD_Ox coating (Fig. 5g–i) proof the presence of relevant residual porosity, due to a lower degree of densification with thermal treatment: the coating, in this case, is thicker (25–30 µm) and the EDX analysis shows slight Cr diffusion in the inner part. However, the EPD_Ox coatings were fully adherent to the SUS 445 substrate with uniform distribution of Co and Mn throughout its thickness.

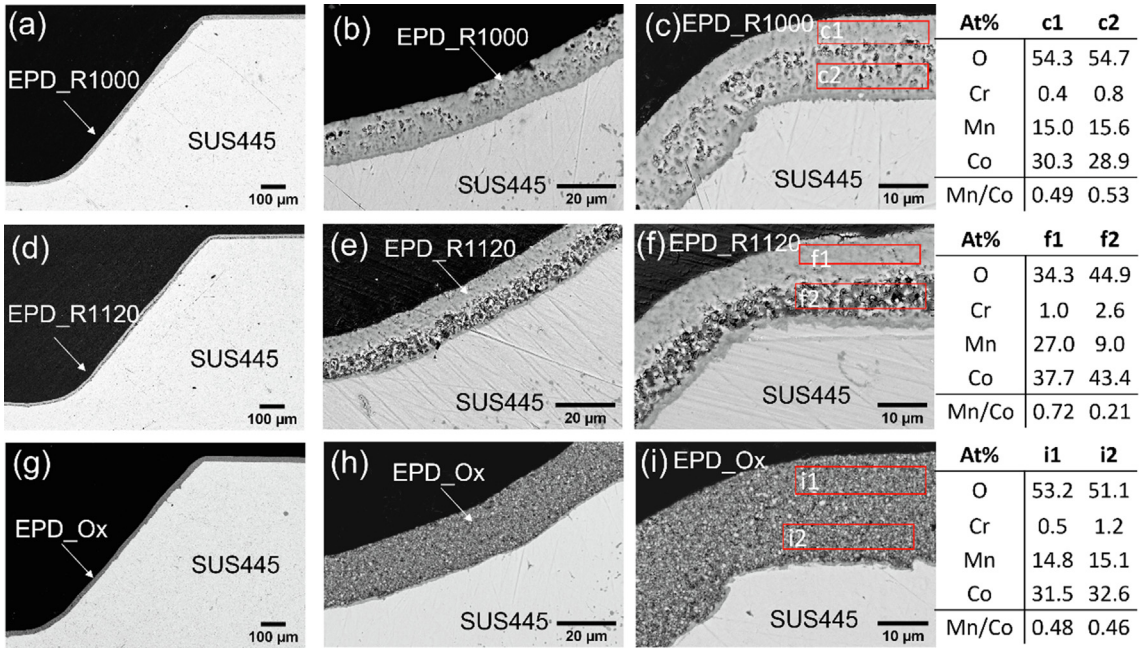

At%	c1	c2
O	54.3	54.7
Cr	0.4	0.8
Mn	15.0	15.6
Co	30.3	28.9
Mn/Co	0.49	0.53

At%	f1	f2
O	34.3	44.9
Cr	1.0	2.6
Mn	27.0	9.0
Co	37.7	43.4
Mn/Co	0.72	0.21

At%	i1	i2
O	53.2	51.1
Cr	0.5	1.2
Mn	14.8	15.1
Co	31.5	32.6
Mn/Co	0.48	0.46

Fig. 5. FE-SEM cross sections images (backscattered electrons) at different magnifications of as sintered EPD coatings after oxidation step and EDX elemental analysis of areas marked in the red colour of EPD_R1000 (a, b, c), EPD_R1120 (d, e, f), EPD_Ox (g, h, i) coatings.

3.2. Area specific resistance

Fig. 6 presents the evolution with time (during 1500 h) of the area specific resistance associated to the 3 different EPD-coated samples measured at 800 °C. Fig. 6 also includes values measured for the uncoated SUS 445 and SUS 445 coated with MC12 by roll painting for comparison. Complementary, Table 2 summarises final resistance values and obtained degradation rates for all interconnects under study.

The uncoated steel shows an ASR value much higher compared than the coated samples. Despite an initial decrease in the resistance, ASR of bare substrates never reached 100 mΩ cm^2, which is considered a threshold for SOC interconnect applications [40,41]. Interestingly, the whole set of EPD deposited samples showed better performance also when compared with the sample coated by conventional methods (RP). The high degradation rate of EPD_Ox coating indicates a possible Cr diffusion phenomenon with the continuous growth of the oxide scale, with higher electrical resistance than the $MnCo_2O_4$ spinel. On the other hand, both EPD coatings subjected to two-step sintering provided the best performance, with low and comparable degradation rates (1.9 and 1.2 mΩ cm^2/kh for EPD_R1120 and EPD_R1000, respectively). Considering the degradation rates measured here for the samples labelled as EPD_R1120 and EPD_R1000, it is possible to extrapolate extremely low ASR values for these ICs after 40 kh of operation (i.e. ≈90 mΩ cm^2 and ≈60 mΩ cm^2, respectively). ASR data obtained in the present work are in good agreement with previously reported values collected from Mn—Co spinel coated stainless steel coupons, obtained by EPD. For example, in the work of Talic et al. [30] undoped, Fe— and Cu-doped $MnCo_2O_4$ EPD coatings revealed a degradation rate in the same range as the present work (1.35 mΩ cm^2/kh at 800 °C). Moreover, a $Mn_{1.5}Co_{1.5}O_4$ spinel coating deposited by EPD and tested at 800 °C for 5000 h showed a degradation rate of 1.2 mΩ cm^2/kh in the study by Molin et al. [25]. However, it is worth noting that small and flat Crofer22APU coupons were used as steel substrate in the previously mentioned works: this special kind of stainless steel is produced by conventional metallurgy methods, involving expensive vacuum remelting to reduce the amount of impurities followed by hot or cold forming. We report here for the first time ASR values for SUS 445 produced by near-net shape powder metallurgy with a complex shape. Compared to Crofer22APU, SUS 445 alloy contains a higher degree of impurities and slightly lower Cr content, which both contribute to lower production costs; the differences in alloy composi-

Table 2
ASR after 1.5 kh of ageing and degradation rate measured at 800 °C in static air.

Sample	ASR after 1.5 kh [mΩ cm^2]	Deg. Rate [mΩ cm^2/kh]
EPD_Ox	30.3	15
EPD_R1120	16.5	1.9
EPD_R1000	12.7	1.2

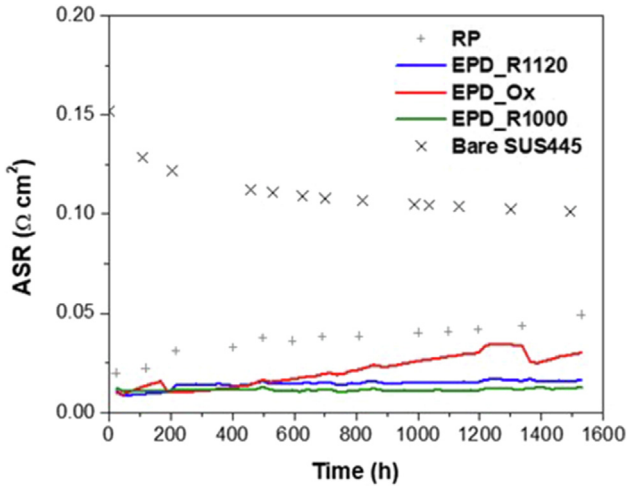

Fig. 6. Evolution of the Area Specific Resistance at 800 °C with time for the different interconnects under study (uncoated bare SUS 445 is included for comparison).

tion should be taken into consideration in the evaluation of test results.

3.3. Post-mortem characterization

Post-mortem characterization of the samples using backscattered electrons imaging is presented in Fig. 7 (together with EDX elemental analysis of marked regions). First, EPD_R1000 coating looks continuous and well attached to the steel substrate. As shown in Fig. 7a, the coating was effective in minimizing surface defects on the interconnect; no cracks are visible, even if pores seem to be more concentrated in the inner part of the coating. EDX analysis reveals that Mn/Co ratio is completely balanced in both the inner and outer parts, while Cr content is found to be almost negligible (<1 at.%). On the other hand, EPD_R1120 coatings maintain the morphology previously observed, i.e. composed by two different layers where the outer part is densified while the inner part is porous (Fig. 7c). Comparing the cross section with the one of the as-prepared sample, the separation between the two zones is here more severe due to pores coalescence during the 1.5 kh ageing at 800 °C, but without spallation. Moreover, vertical cracks are clearly observed, especially in the convex edges of the steel interconnect, as reported in the Fig. 7c. Crack formation is a sign of the presence of thermo-mechanical stresses in the coating that may lead to mechanical failure during the cooling down or the thermal cycling. Obtaining a highly dense coating is considered the most efficient way to block Cr diffusion from the steel interconnect. However, the formation of the described double-layer morphology might arise detrimental consequences due to the inhomogeneous microstructure of the coating. The Mn/Co ratio in the outer and inner parts of the coatings shows perfectly balanced elements distribution, which proves that the continuous oxidation during the ASR test at 800 °C promoted Mn and Co interdiffusion, restoring initial MC12 stoichiometry, despite notable inhomogeneity found in as-prepared samples (Fig. 5f). To summarise, after the ASR test (1500 h at 800 °C) the uneven densification of the coatings subjected to the two-step sintering is confirmed, with further densification occurred during ageing. This effect is more visible for EPD_R1120 than for EPD_R1000 samples.

Finally, images of the EPD_Ox sample in Fig. 7e and f describe a similar morphology compared to the as-prepared samples. The coating still appears highly porous, but with a well densified layer at the interface with the steel substrate (around 5 μm-thick). Mn and Co are present in stoichiometric amounts; moreover, Cr concentration is >1 at.% in the coating, reaching almost 2 at.% in the inner part. Indeed, Mn—Co spinel coating subjected to one-step sintering in air does not reach a satisfactory densification level and is, therefore, unable to block Cr diffusion and evaporation from the steel.

According to morphological results collected so far on the aged samples, there is no evidence of possible different oxidation mechanism occurring between the flat surfaces or edges of the coated interconnects. It is also important to discuss that in the EPD coated interconnects, the major stress concentration has been proved to be at the concave zones; therefore, the design of the curvature radius plays a key role, especially in those areas [26]. In the case of SUS 445 interconnects of the present study, the radius of the concave areas is large enough to avoid the mentioned issue in all three groups of samples, this in addition to the high degree of conformity offered by EPD. Only the sample EPD_R1120 exhibits cracks in coating at the convex edges, which indicates that chosen sintering parameters caused excessive stress accumulation, espe-

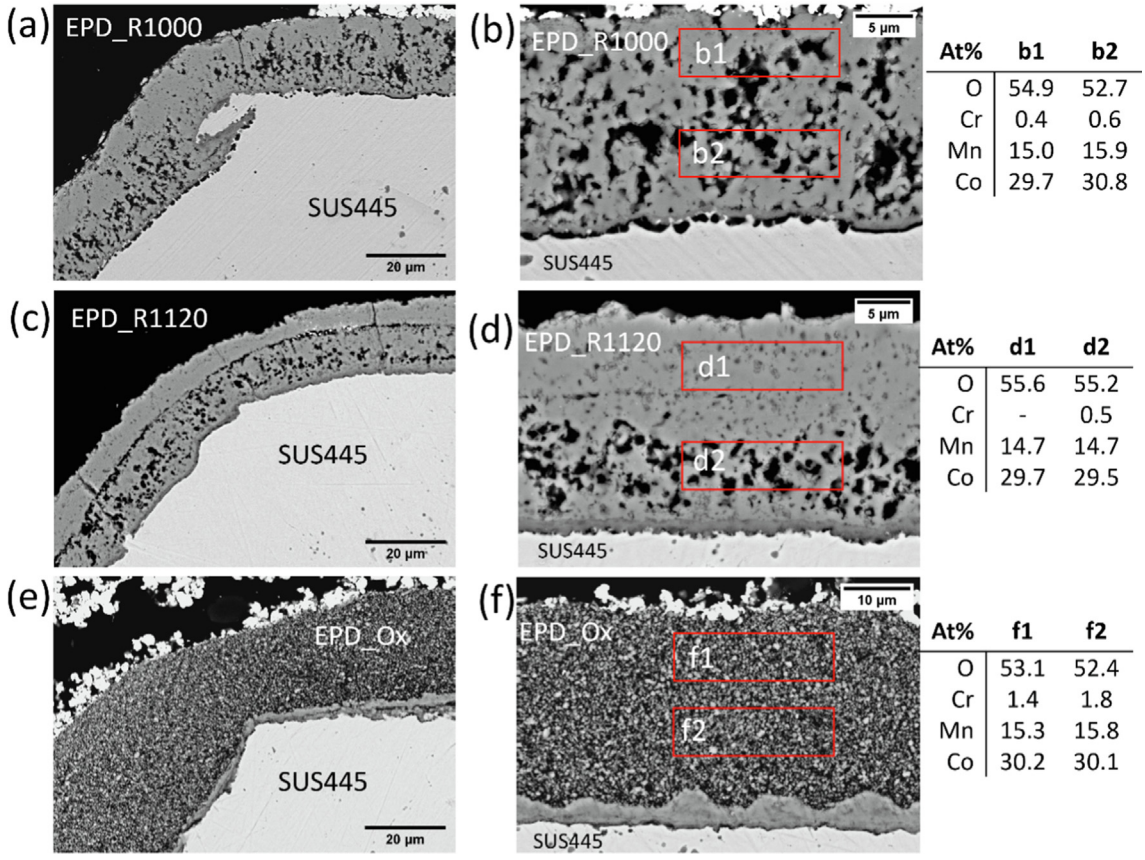

At%	b1	b2
O	54.9	52.7
Cr	0.4	0.6
Mn	15.0	15.9
Co	29.7	30.8

At%	d1	d2
O	55.6	55.2
Cr	-	0.5
Mn	14.7	14.7
Co	29.7	29.5

At%	f1	f2
O	53.1	52.4
Cr	1.4	1.8
Mn	15.3	15.8
Co	30.2	30.1

Fig. 7. FE-SEM cross sections images (backscattered electrons) at different magnifications of EPD coatings after 1500 h ASR test at 800 °C and EDX elemental analysis of areas marked in red colour: EPD_R1000 (a, b), EPD_R1120 (c, d), EPD_Ox (e, f).

cially due to the development of the double-layer morphology of the MC12 coating. On the other hand, it is relevant to note that the same type of cracks was not observed for the EPD_R1000 and EPD_Ox samples. Considering all the mentioned aspects, the results reported in the present study represent the first step towards the integration of sustainable processing approaches like powder metallurgy and electrophoretic deposition in the field of SOC metallic interconnects together with the importance of integrating an effective coating deposition method with the IC produced via PM.

Fig. 8 shows images at higher magnification of the steel/coating interface of the three variants of EPD coatings after the ASR test; EDX quantitative analysis of marked points is reported in Table 3. While comparing the figures, it is possible to observe different morphologies of the interfaces. In the case of EPD_R1000 samples in Fig. 8a, a thin (<1 μm) chromia scale is formed. Moreover, it is evident that Si-rich nodules developed in the sub-scale area (point a2). A low concentration of Si is also detected in the chromia (point a1). Silicon is present in the stainless steel in low concentrations (<0.5 %) as alloy impurity and can apparently accumulate at the steel interface during long term ageing at high temperature. The presence of this sub-scale oxide could strongly affect the electrical conductivity of the system, but interestingly, EPD_R1000 samples provided the best results in terms of ASR.

The sample labelled EPD_R1120 (Fig. 8b) shows a continuous coating/steel interface, despite the high porosity of the coating in the inner area. However, a chromia layer (point b2) with a thickness between 1.5 and 2.0 μm is formed during ageing and a Si-rich layer is detected (also by EDX in point b3) in the sub-scale area. Chromium is slightly diffused into the coating forming a reaction layer pointed out in EDX point b1; the thickness of the reaction layer is difficult to assess, as the Cr concentration in the coating layer goes rapidly down to an undetectable level, as already shown in Fig. 7d.

It is interesting to discuss the unexpected morphology of the EPD_Ox sample interface shown in Fig. 8c: the interface between the coating and the steel substrate is composed of a first scale layer composed of Si, Cr and Fe (point c2), followed by a second layer formed by diffusion of both Cr and Fe in the Co—Mn spinel coating (point c1). The reaction layer in this case results in 3–4 μm thick and fully dense; its formation justifies the highest ASR value as well as degradation rate compared to other EPD coated samples.

The presence of silica at the oxide scale between the steel and the coating determines the development of a weak interface, with possible crack formation and delamination phenomena. Similar behaviour was observed for EPD-coated, Si containing AISI 441 alloy when tested at 750 °C for 3200 h for ASR monitoring [34]. Compared to AISI 441, SUS 445 does not contain Nb, a Laves phase forming element in charge of reducing silica formation [42,43]; this could clarify the evident silicon-rich oxides accumulation at the steel surface after oxidation, as seen for the three sets of samples here described, even if with different features. Moreover, SUS 445 does not contain any alloying elements which could improve the adhesion of the oxide scale. Indeed, rare earth elements (like La, Y, Ce) can be included as alloying elements in a small amount (0.1–0.2 %) as they have been demonstrated to improve the adhesion of the oxide scale and to decrease the oxidation rate [44]; this is a common feature of special alloys developed for interconnects, such as Crofer22APU. Therefore, it is suggested that a fine adjustment on SUS 445 alloy composition could lead to a significant improvement in the long-term performance of EPD coated interconnects.

To summarize, the morphological results just discussed prove that the choice of the coating sintering routes remarkably affects the electrical behaviour of coated interconnects here investigated. The activation of different interactions between the coating and the steel substrate over ageing is mostly appreciable when coatings subjected to one-step or two-step sintering are compared; however, for coatings exposed to two-step sintering, substantial variation of oxidation phenomena appears when the parameters of the first heat treatment in reducing atmosphere are modified.

4. Conclusions

The present work assesses the use of SOC interconnects produced by powder metallurgy with cost-effective SUS 445 ferritic stainless steel and coated by EPD technique with $MnCo_2O_4$ spinel. The results indicate that the EPD deposition method is effective for coating complex surfaces and that the parameters of the reducing treatment have significant influences on the final microstructures of the studied coating and their measured electrical properties. The optimal sintering treatment is based on a reduction step at 1000 °C followed by a re-oxidation at 800 °C in air. The best performing IC presents a very low specific resistance of 12.7 mΩ cm^2 after 1500 h at 800 °C, with degradation rate below 1.2 mΩ cm^2/kh. The current study presents new insights into the increasing use of EPD as a reliable and scalable coating solution to reduce degradation phenomena in SOCs. Furthermore, it lays the groundwork for possible integration and synergy between the powder metallurgy approach and the electrophoretic deposition, which, combined, represent a cheap and scalable solution for complex-shaped interconnects for high-temperature solid oxide cell applications. The effective combination between PM and EPD could lead to a decrease in processing times that can be translated into a reduction of costs of SOC stack, which is a key achievement for the full commercialization of this technology.

CRediT authorship contribution statement

Elisa Zanchi: Investigation, Writing – original draft, Visualization, Data curation, Conceptualization, Validation. **Antonio Gianfranco Sabato:** Investigation, Writing – review & editing, Visualization, Data curation, Conceptualization, Methodology. **Mari Carmen Monterde:** Investigation, Conceptualization, Visualization, Writing – review & editing. **Lucile Bernadet:** Investigation, Conceptualization. **Marc Torrell:** Conceptualization, Methodology,

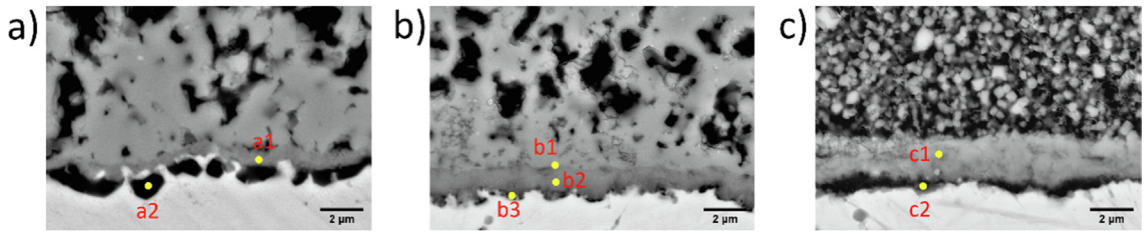

Fig. 8. FE-SEM cross sections images (backscattered electrons) of steel substrate/EPD coatings interface after ASR test: EPD_R1000 (a), EPD_R1120 (b), EPD_Ox (c). EDX elemental analysis of points marked in the yellow colour is reported in Table 3.

Table 3
EDX elemental analysis of points marked in Fig. 8.

Sample	Point	O (at.%)	Si (at.%)	Cr (at.%)	Mn (at.%)	Fe (at.%)	Co (at.%)
EPD_R1000	a1	57.6	1.4	34.2	1.1	3.6	2.0
	a2	54.1	18.4	9.2	0.5	18.8	–
EPD_R1120	b1	57.2	–	5.4	12.4	–	25.0
	b2	63.7	–	24.1	7.8	2.9	1.5
	b3	52.5	5.5	19.5	3.5	18.3	0.6
EPD_Ox	c1	40.1	–	4.6	18.8	1.3	35.3
	c2	64.8	7.2	17.5	1.9	7.5	1.1

Writing – review & editing, Supervision. **José Antonio Calero:** Conceptualization, Resources, Supervision. **Albert Tarancón:** Conceptualization, Methodology, Resources, Writing – review & editing, Supervision, Project administration. **Federico Smeacetto:** Conceptualization, Writing – review & editing, Resources, Supervision, Project administration.

Data availability

Data will be made available on request.

Declaration of Competing Interest

The authors declare that they have no known competing financial interests or personal relationships that could have appeared to influence the work reported in this paper.

Acknowledgements

The authors also want to acknowledge the financial support of the "Generalitat de Catalunya" through AGAUR for the Industrial PhD ref.2017 DI 035 and NANOEN (2017 SGR 1421). The research leading to these results has received funding from DEFINE-SOEC (n° ACE034/21/000001) project. The experimental work of MSc Federica Geraci and MSc Alberto Poli is kindly acknowledged.

References

[1] L. van Biert, K. Visser, P.V. Aravind, A comparison of steam reforming concepts in solid oxide fuel cell systems, Appl. Energy. 264 (2020), https://doi.org/10.1016/j.apenergy.2020.114748 114748.
[2] M.B. Mogensen, M. Chen, H.L. Frandsen, C. Graves, J.B. Hansen, K.V. Hansen, A. Hauch, T. Jacobsen, S.H. Jensen, T.L. Skafte, X. Sun, Reversible solid-oxide cells for clean and sustainable energy, Clean Energy. 3 (2019) 175–201, https://doi.org/10.1093/ce/zkz023.
[3] N. Mahato, A. Banerjee, A. Gupta, S. Omar, K. Balani, Progress in material selection for solid oxide fuel cell technology: A review, Prog. Mater. Sci. 72 (2015) 141–337, https://doi.org/10.1016/j.pmatsci.2015.01.001.
[4] A. Nechache, S. Hody, Alternative and innovative solid oxide electrolysis cell materials: A short review, Renew. Sustain. Energy Rev. 149 (2021), https://doi.org/10.1016/j.rser.2021.111322.
[5] N.S. Mohd Affandi, N. Osman, Short review on global trends in SOFC scenario and future perspective, Mater. Today Proc. (2022), https://doi.org/10.1016/j.matpr.2022.04.824.
[6] S. Zarabi Golkhatmi, M.I. Asghar, P.D. Lund, A review on solid oxide fuel cell durability: Latest progress, mechanisms, and study tools, Renew. Sustain. Energy Rev. 161 (2022), https://doi.org/10.1016/j.rser.2022.112339 112339.
[7] W.J. Quadakkers, J. Piron-Abellan, V. Shemet, L. Singheiser, Metallic interconnectors for solid oxide fuel cells – a review, Mater. High Temp. 20 (2003) 115–127, https://doi.org/10.1179/mht.2003.015.
[8] M.A. Hassan, O. Bin Mamat, M. Mehdi, Review: Influence of alloy addition and spinel coatings on Cr-based metallic interconnects of solid oxide fuel cells, Int. J. Hydrogen Energy. 45 (2020) 25191–25209, https://doi.org/10.1016/j.ijhydene.2020.06.234.
[9] C.M. Harrison, P.R. Slater, R. Steinberger-Wilckens, A review of solid oxide fuel cell cathode materials with respect to their resistance to the effects of chromium poisoning, Solid State Ionics. 354 (2020), https://doi.org/10.1016/j.ssi.2020.115410 115410.
[10] M. Bianco, J.P. Ouweltjes, J. Van herle, Degradation analysis of commercial interconnect materials for solid oxide fuel cells in stacks operated up to 18000 hours, Int. J. Hydrogen Energy. 44 (2019) 31406–31422, https://doi.org/10.1016/j.ijhydene.2019.09.218.
[11] Z. Zhou, V.K. Nadimpalli, D.B. Pedersen, V. Esposito, Degradation mechanisms of metal-supported solid oxide cells and countermeasures: A review, Materials (Basel). 14 (2021), https://doi.org/10.3390/ma14113139.
[12] J. Mikkola, K. Couturier, B. Talic, S. Frangini, N. Giacometti, N. Pelissier, B.R. Sudireddy, O. Thomann, Protective coatings for ferritic stainless steel interconnect materials in high temperature solid oxide electrolyser atmospheres, Energies. 15 (2022), https://doi.org/10.3390/en15031168.
[13] J.C.W. Mah, A. Muchtar, M.R. Somalu, M.J. Ghazali, Metallic interconnects for solid oxide fuel cell: A review on protective coating and deposition techniques, Int. J. Hydrogen Energy. 42 (2017) 9219–9229, https://doi.org/10.1016/j.ijhydene.2016.03.195.
[14] J.H. Zhu, D.A. Chesson, Y.T. Yu, Review—(Mn, Co) 3 O 4-based spinels for SOFC interconnect coating application, J. Electrochem. Soc. 168 (2021), https://doi.org/10.1149/1945-7111/ac3a29 114519.
[15] K.H. Tan, H.A. Rahman, H. Taib, Coating layer and influence of transition metal for ferritic stainless steel interconnector solid oxide fuel cell: A review, Int. J. Hydrogen Energy. 44 (2019) 30591–30605, https://doi.org/10.1016/j.ijhydene.2019.06.155.
[16] J.G. Grolig, J. Froitzheim, J.E. Svensson, Coated stainless steel 441 as interconnect material for solid oxide fuel cells: Evolution of electrical properties, J. Power Sources. 284 (2015) 321–327, https://doi.org/10.1016/j.jpowsour.2015.03.029.
[17] P. Alnegren, M. Sattari, J.E. Svensson, J. Froitzheim, Temperature dependence of corrosion of ferritic stainless steel in dual atmosphere at 600–800 °C, J. Power Sources. 392 (2018) 129–138, https://doi.org/10.1016/j.jpowsour.2018.04.088.
[18] B. Talic, V. Venkatachalam, P.V. Hendriksen, R. Kiebach, Comparison of MnCo2O4 coated Crofer 22 H, 441, 430 as interconnects for intermediate-temperature solid oxide fuel cell stacks, J. Alloys Compd. 821 (2020), https://doi.org/10.1016/j.jallcom.2019.153229 153229.
[19] A. Bakhshi-Zadeh, S. Salmani, M.A. Faghihi-Sani, H. Abdoli, N. Jalili, Oxidation behavior and electrical properties of de-siliconized AISI 430 alloy with Mn1.5Co1.5O4 coating for solid oxide fuel cell interconnect, Oxid. Met. 93 (2020) 401–415, https://doi.org/10.1007/s11085-020-09962-x.
[20] T. Thublaor, S. Chandra-ambhorn, High temperature oxidation and chromium volatilisation of AISI 430 stainless steel coated by Mn-Co and Mn-Co-Cu oxides for SOFC interconnect application, Corros. Sci. 174 (2020), https://doi.org/10.1016/j.corsci.2020.108802 108802.
[21] V. Kruzhanov, V. Arnhold, Energy consumption in powder metallurgical manufacturing, Powder Metall. 55 (2012) 14–21, https://doi.org/10.1179/174329012X13318077875722.
[22] A. Topcu, B. Öztürk, Ö.N. Cora, Performance evaluation of machined and powder metallurgically fabricated Crofer®22 APU interconnects for SOFC applications, Int. J. Hydrogen Energy. 47 (2022) 3437–3448, https://doi.org/10.1016/j.ijhydene.2021.06.036.
[23] I. Antepara, I. Villarreal, L.M. Rodríguez-Martínez, N. Lecanda, U. Castro, A. Laresgoiti, Evaluation of ferritic steels for use as interconnects and porous metal supports in IT-SOFCs, J. Power Sources. 151 (2005) 103–107, https://doi.org/10.1016/j.jpowsour.2005.02.084.
[24] B. Öztürk, A. Topcu, S. Öztürk, Ö.N. Cora, Oxidation, electrical and mechanical properties of Crofer®22 solid oxide fuel cell metallic interconnects manufactured through powder metallurgy, Int. J. Hydrogen Energy. 43 (2018) 10822–10833, https://doi.org/10.1016/j.ijhydene.2018.01.078.
[25] S. Molin, A.G. Sabato, M. Bindi, P. Leone, G. Cempura, M. Salvo, S. Cabanas Polo, A.R. Boccaccini, F. Smeacetto, Microstructural and electrical characterization of Mn-Co spinel protective coatings for solid oxide cell interconnects, J. Eur. Ceram. Soc. 37 (2017) 4781–4791, https://doi.org/10.1016/j.jeurceramsoc.2017.07.011.
[26] B. Talic, A.C. Wulff, S. Molin, K.B. Andersen, P. Zielke, H.L. Frandsen, Investigation of electrophoretic deposition as a method for coating complex shaped steel parts in solid oxide cell stacks, Surf. Coatings Technol. 380 (2019) 1–8, https://doi.org/10.1016/j.surfcoat.2019.125093.
[27] E. Zanchi, A.G. Sabato, S. Molin, G. Cempura, A.R. Boccaccini, F. Smeacetto, Recent advances on spinel-based protective coatings for solid oxide cell metallic interconnects produced by electrophoretic deposition, Mater. Lett. 286 (2021), https://doi.org/10.1016/j.matlet.2020.129229 129229.
[28] I. Aznam, J.C.W. Mah, A. Muchtar, M.R. Somalu, M.J. Ghazali, Electrophoretic deposition of (Cu, Mn, Co)3O4 spinel coating on SUS430 ferritic stainless steel: Process and performance evaluation for solid oxide fuel cell interconnect applications, J. Eur. Ceram. Soc. 41 (2021) 1360–1373, https://doi.org/10.1016/j.jeurceramsoc.2020.09.074.

[29] S.U. Oh, D. Kim, I.T. Lee, C.S. Choi, J.A. Lee, Y.W. Heo, J.H. Lee, Electrophoretic deposition and low-temperature densification of Cu1.35Mn1.65O4 spinel for an interconnect protective coating in solid oxide fuel cells, Int. J. Hydrogen Energy. 47 (2022) 33410–33419, https://doi.org/10.1016/j.ijhydene.2022.07.259.
[30] B. Talic, S. Molin, K. Wiik, P.V. Hendriksen, H.L. Lein, Comparison of iron and copper doped manganese cobalt spinel oxides as protective coatings for solid oxide fuel cell interconnects, J. Power Sources. 372 (2017) 145–156, https://doi.org/10.1016/j.jpowsour.2017.10.060.
[31] E. Zanchi, J. Ignaczak, S. Molin, G. Cempura, A.R. Boccaccini, F. Smeacetto, Electrophoretic co-deposition of Mn1.5Co1.5O4, Fe2O3 and CuO: Unravelling the effect of simultaneous addition of Cu and Fe on the microstructural, thermo-mechanical and corrosion properties of in-situ modified spinel coatings for solid oxide cell intercon, J. Eur. Ceram. Soc. 42 (2022) 3271–3281, https://doi.org/10.1016/j.jeurceramsoc.2022.02.008.
[32] A.G. Sabato, S. Molin, H. Javed, E. Zanchi, A.R. Boccaccini, F. Smeacetto, In-situ Cu-doped MnCo-spinel coatings for solid oxide cell interconnects processed by electrophoretic deposition, Ceram. Int. 45 (2019) 19148–19157, https://doi.org/10.1016/j.ceramint.2019.06.161.
[33] E. Zanchi, B. Talic, A.G. Sabato, S. Molin, A.R. Boccaccini, F. Smeacetto, Electrophoretic co-deposition of Fe2O3 and Mn1,5Co1,5O4: Processing and oxidation performance of Fe-doped Mn-Co coatings for solid oxide cell interconnects, J. Eur. Ceram. Soc. 39 (2019) 3768–3777, https://doi.org/10.1016/j.jeurceramsoc.2019.05.024.
[34] E. Zanchi, S. Molin, A.G. Sabato, B. Talic, G. Cempura, A.R. Boccaccini, F. Smeacetto, Iron doped manganese cobaltite spinel coatings produced by electrophoretic co-deposition on interconnects for solid oxide cells: Microstructural and electrical characterization, J. Power Sources. 455 (2020), https://doi.org/10.1016/j.jpowsour.2020.227910 227910.
[35] A.G. Sabato, E. Zanchi, S. Molin, G. Cempura, H. Javed, K. Herbrig, C. Walter, A.R. Boccaccini, F. Smeacetto, Mn-Co spinel coatings on Crofer 22 APU by electrophoretic deposition: Up scaling, performance in SOFC stack at 850 °C and compositional modifications, J. Eur. Ceram. Soc. 41 (2021) 4496–4504, https://doi.org/10.1016/j.jeurceramsoc.2021.03.030.
[36] E. Zanchi, J. Ignaczak, B. Kamecki, P. Jasiński, S. Molin, A.R. Boccaccini, F. Smeacetto, Manganese-cobalt based spinel coatings processed by electrophoretic deposition method: The influence of sintering on degradation issues of solid oxide cell oxygen electrodes at 750 °C, Materials (Basel). 14 (2021) 3836, https://doi.org/10.3390/ma14143836.
[37] M. Bobruk, S. Molin, M. Chen, T. Brylewski, P.V. Hendriksen, Sintering of MnCo2O4 coatings prepared by electrophoretic deposition, Mater. Lett. 213 (2018) 394–398, https://doi.org/10.1016/j.matlet.2017.12.046.
[38] S. Gates-Rector, T. Blanton, The powder diffraction file: A quality materials characterization database, Powder Diffr. 34 (2019) 352–360, https://doi.org/10.1017/S0885715619000812.
[39] B. Talic, H. Falk-Windisch, V. Venkatachalam, P.V. Hendriksen, K. Wiik, H.L. Lein, Effect of coating density on oxidation resistance and Cr vaporization from solid oxide fuel cell interconnects, J. Power Sources. 354 (2017) 57–67, https://doi.org/10.1016/j.jpowsour.2017.04.023.
[40] J.W. Fergus, Metallic interconnects for solid oxide fuel cells, Mater. Sci. Eng. A. 397 (2005) 271–283, https://doi.org/10.1016/j.msea.2005.02.047.
[41] W.Z. Zhu, S.C. Deevi, Opportunity of metallic interconnects for solid oxide fuel cells: A status on contact resistance, Mater. Res. Bull. 38 (2003) 957–972, https://doi.org/10.1016/S0025-5408(03)00076-X.
[42] B. Kuhn, C.A. Jimenez, L. Niewolak, T. Hüttel, T. Beck, H. Hattendorf, L. Singheiser, W.J. Quadakkers, Effect of Laves phase strengthening on the mechanical properties of high Cr ferritic steels for solid oxide fuel cell interconnect application, Mater. Sci. Eng. A. 528 (2011) 5888–5899, https://doi.org/10.1016/j.msea.2011.03.112.
[43] T. Horita, H. Kishimoto, K. Yamaji, Y. Xiong, N. Sakai, M.E. Brito, H. Yokokawa, Evaluation of laves-phase forming Fe-Cr alloy for SOFC interconnects in reducing atmosphere, J. Power Sources. 176 (2008) 54–61, https://doi.org/10.1016/j.jpowsour.2007.10.041.
[44] H.S. Seo, G. Jin, J.H. Jun, D.H. Kim, K.Y. Kim, Effect of reactive elements on oxidation behaviour of Fe-22Cr-0.5Mn ferritic stainless steel for a solid oxide fuel cell interconnect, J. Power Sources. 178 (2008) 1–8, https://doi.org/10.1016/j.jpowsour.2007.12.026.